



Modulation of Boundary-Layer Stability and the Surface Energy Budget by a Local Flow in Central Alaska

Julia Maillard¹ · François Ravetta¹ · Jean-Christophe Raut¹ ·
Gilberto J. Fochesatto² · Kathy S. Law¹

Received: 12 November 2021 / Accepted: 25 July 2022 / Published online: 27 August 2022
© The Author(s) 2022

Abstract

The pre-ALPACA (Alaskan Layered Pollution And Chemical Analysis) 2019 winter campaign took place in Fairbanks, Alaska, in November–December 2019. One objective of the campaign was to study the life-cycle of surface-based temperature inversions and the associated surface energy budget changes. Several instruments, including a 4-component radiometer and sonic anemometer were deployed in the open, snow-covered University of Alaska Fairbanks (UAF) Campus Agricultural Field. A local flow from a connecting valley occurs at this site. This flow is characterized by locally elevated wind speeds (greater than 3 m s^{-1}) under clear-sky conditions and a north-westerly direction. It is notably different to the wind observed at the airport more than 3.5 km to the south-west. The surface energy budget at the UAF Field site exhibits two preferential modes. In the first mode, turbulent sensible heat and net longwave fluxes are close to 0 W m^{-2} , linked to the presence of clouds and generally low winds. In the second, the net longwave flux is around -50 W m^{-2} and the turbulent sensible heat flux is around 15 W m^{-2} , linked to clear skies and elevated wind speeds. The development of surface-based temperature inversions at the field is hindered compared to the airport because the local flow sustains vertical mixing. In this second mode the residual of the surface energy budget is large, possibly due to horizontal temperature advection.

Keywords High latitude · Local flow · Surface energy budget · Surface temperature inversion · Winter

1 Introduction

Surface-based temperature inversions (SBIs) are a ubiquitous feature of the Arctic winter atmosphere, occurring as often as 70% of the time (Serreze et al. 1992; Bradley et al. 1992). The study of these inversions is motivated in two ways. Firstly, they have important implications for air pollution in the Arctic. Surface-based temperature inversions ‘trap’ emissions

✉ Julia Maillard
julia.maillard@latmos.ipsl.fr

¹ LATMOS/IPSL, Sorbonne Université, UVSQ, CNRS, 4 place Jussieu, 75005 Paris, France

² Department of Atmospheric Sciences, College of Natural Science and Mathematics, University of Alaska Fairbanks, 1930 Yukon Drive, P.O. Box 755940, Fairbanks, AL 97775-5904, USA

from surface sources by imposing a shallow stratified layer close to the surface. Combined with low horizontal winds, this can lead to an accumulation of pollutants near the surface. For example, SBIs in Fairbanks, Alaska, are such that the temperature at 30 m is often 5 K higher than that at 2 m (Mayfield and Fochesatto 2013; Malingowski et al. 2014). Fairbanks is therefore regularly classified as a non-attainment zone according to the PM_{2.5} National Ambient Air Quality Standard. Secondly, strong SBIs have been shown to confine the warming caused by climate change to the surface, while increased vertical mixing is linked to a dilution of the warming to higher altitudes (Bintanja et al. 2011). This mechanism, termed ‘lapse-rate feedback’, is a major contributor to Arctic Amplification (Pithan and Mauritsen 2014).

In the Arctic winter, the presence of snow-covered, emissive surfaces combined with the absence of incoming shortwave radiation leads to longwave radiative cooling becoming the main contributor to the surface energy budget. This effect is particularly large in anticyclonic conditions when clouds and surface winds are inhibited. In these conditions, a ‘very stable’ regime often develops: turbulent heat fluxes are small and the lowest layer of the atmosphere cools rapidly, creating an SBI. As surface stability increases, vertical motions are suppressed. This then further reduces the turbulent heat flux. The ensuing positive feedback loop leads to a sharply increasing temperature profile, and the surface being thermally and mechanically decoupled from the overlying atmosphere (van Hooijdonk et al. 2015).

Alternatively, the boundary layer may operate in a ‘weakly stable’ regime, in which the wind speed is sufficient to maintain a turbulent sensible heat flux which compensates the radiative cooling. These two regimes have been shown to be separated by a critical wind speed, termed ‘minimum wind speed for sustainable turbulence’ (van de Wiel et al. 2012; van Hooijdonk et al. 2015). A conceptual model of the surface-based temperature inversion under these two regimes was developed by van de Wiel et al. (2017), and the existence of these two distinct regimes separated by a sharp transition was confirmed at Cabauw in the Netherlands (van Hooijdonk et al. 2015) and Dome C in Antarctica (Vignon et al. 2017).

Surface-based temperature inversions are common and have long been studied in Fairbanks, the main population centre of Interior Alaska. By calculating monthly averages of radiosonde profiles from 1957–2008, Bourne et al. (2010) found that SBIs occurred 60–80% of the time in November and December, with a temperature difference across the inversion of 7.5–10.5 °C and an inversion depth of 500–550 m. Mayfield and Fochesatto (2013), on the other hand, differentiated between SBIs and elevated inversions, taking into account the frequent layering of individual radiosonde profiles. They found an SBI occurrence frequency of 64% for the months of October–March from 2000–2009. Fairbanks is situated in the Tanana Valley and is surrounded on three sides by hills. These hills are separated by valleys, one of which (Goldstream) connects directly to the Tanana Valley on the north-west edge of Fairbanks (Fig. 1). This topography means that a local scale circulation, termed ‘shallow cold flow’ (SCF), is often observed under anticyclonic synoptic conditions (Fochesatto et al. 2013).

While the development of strong SBIs is often driven by high pressures and clear skies, they can also potentially be impacted by the local circulations, which develop when anticyclonic conditions prevail in the region. Previous studies have explored the variability of nocturnal stability conditions caused by local flows in the mid-latitudes. Martínez et al. (2010), for example, made use of an extensive dataset to link the flow in a wide basin in Northern Spain to the nocturnal cooling rate. Mahrt et al. (2001), using data from CASES-99 field campaign (in Leon, Kansas), showed that strongly stable conditions develop at the beginning of the night in a shallow gully, accompanied by a very weak, shallow flow. Influences of regional scale meteorology and valley flows on SBIs have also been reported in the Alps (Rotach

et al. 2004; Haid et al. 2021). In the present paper, the impact of a local flow on SBIs and the surface energy balance at a high-latitude site in the winter is explored, with the ensuing specificity that stability is developed over the course of a few days rather than hours if the synoptic conditions remain favourable.

First, the 2019 pre-ALPACA (Alaskan Layered Pollution And Chemical Analysis) winter campaign in Fairbanks, Alaska and the resulting dataset are presented (Sect. 2). Second, a case study is presented in which a strong SBI was caused by favourable synoptic conditions at the Fairbanks International Airport, but not at the campaign measurement site some 3.5 km away. This indicates that there is local variability in the development of SBIs in Fairbanks (Sect. 3). All the campaign data is then used to show that a local flow, which is enhanced under clear-sky conditions, exists at the measurement site, and to explore its impact on the surface-based temperature inversions and energy balance (Sect. 4). Conclusions are presented in Sect. 5.

2 Pre-ALPACA Winter 2019 Campaign

2.1 Campaign Goals and Theoretical Framework

A pre-ALPACA winter campaign took place in November–December 2019 in Fairbanks (Alaska). It was led by researchers from six French laboratories and the University of Alaska Fairbanks (UAF) and acted as a preliminary run to the main ALPACA campaign, set to take place in January–February 2022 as part of the PACES (air Pollution in the Arctic: Climate, Environment and Societies) International Global Atmospheric Chemistry (IGAC) and International Arctic Science Committee (IASC) initiative (Simpson et al. 2019).

The aim of the pre-ALPACA campaign was to gain some first insights into the processes influencing the formation of wintertime pollution episodes. Fairbanks regularly encounters high aerosol loadings in winter due to high local emissions and stable weather conditions. As well as investigating aerosol formation in dark, cold winter conditions, another crucial goal of the campaign was to study processes influencing the formation of strongly stable surface conditions, as they impact the dispersion of surface emissions. This paper presents an analysis of the energy fluxes and meteorological measurements from the 2019 campaign with a focus on the life cycle of surface-based temperature inversions.

First, the theoretical framework, notations and conventions used for the energy budget are introduced. The studied system consists of the air layer below the instrument height (2 m) and a snow layer of depth $d_s \approx 33 \pm 1$ cm as measure with a ruler (Fig. 2). The snow is conceptually separated into two layers. The top one (1), of height h_s , is thin and is assumed to have the same temperature as the snow–air interface (i.e., the surface). It therefore stores energy by warming and cooling rapidly. The bottom one (2) is assumed to vary more slowly in temperature, and is therefore considered to be an ‘insulation’ layer which transfers the heat conductively from the ground to the surface. This is supported by Helgason and Pomeroy (2012), where it was shown that the first few centimetres of the snowpack follow very similar temperature evolutions to the surface, while the bottom of the snowpack varies much more slowly in temperature. This approach allows us to take into account the energy storage in the snowpack. The energy budget applied to the air layer and snow layer (1) is therefore:

$$S_a + S_s = R_n + H + G + L + \delta E. \quad (1)$$

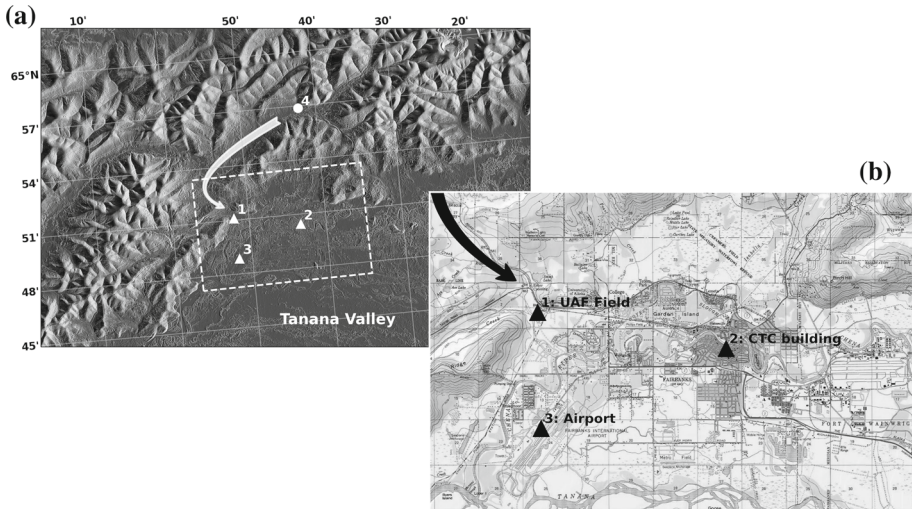


Fig. 1 Map of the measurement sites during the pre-ALPACA 2019 campaign, within the wider topographic context of the Fairbanks basin (a), and zoomed to show the city layout (b). The triangles 1–3 mark the main measurement sites: the UAF Field site, the CTC building, and the Fairbanks airport respectively. The dot marked “4” indicates the location of the Goldstream valley. The white and black arrows show the proposed direction of a local flow from the Goldstream to the Tanana valley, where Fairbanks is located. The elevation data used to generate (a) are the Alaska IFSAR 5 m DEM dataset, downloaded from the USGS National Map website: <https://apps.nationalmap.gov/downloader/>. (b) is an USGS Topo map, taken from the TopoView website: <https://ngmdb.usgs.gov/topoview/viewer/>

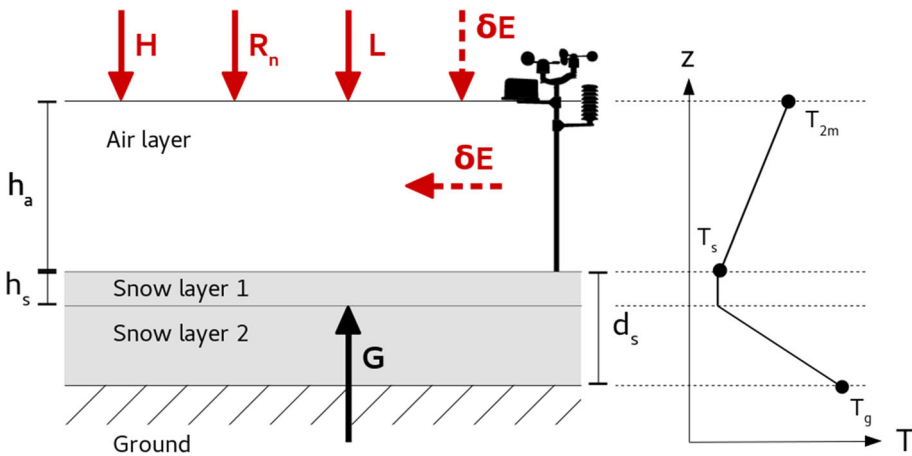


Fig. 2 Schematic of the studied system, which consists of an air layer, a snow layer (which is conceptually divided in two), and the ground. The top of the air layer corresponds to the instrument installation height, $h_a = 2$ m. $d_s \approx 33$ cm is the total snow depth, while h_s is the height of the thin snow layer which closely follows the surface temperature changes. T_{2m} is the air temperature at 2 m, T_s is the surface temperature, and T_g the ground temperature. The downwelling fluxes H , R_n , and L are indicated in red, and the conductive flux through the ground G is shown in black. δE is the surface energy balance residual

The left-hand side of this equation is the heat storage in the air (S_a) and first snow layers (S_s). Because of the very low heat capacity of air, around $1005 \text{ J K}^{-1} \text{ kg}^{-1}$, S_a is negligible compare to S_s and its calculation will not be detailed. The heat storage in the first snow layer can be calculated as:

$$S_s = \rho_s C_{p,s} h_s \frac{\partial T_S}{\partial t}, \quad (2)$$

where $\rho_s = 290 \text{ kg m}^{-3}$ is the snow density, $C_{p,s} = 2 \text{ J K}^{-1} \text{ g}^{-1}$ the specific heat of snow, and T_S the temperature of the snow–air interface, measured by the radiometer (Eq. 4). The snow density and specific heat capacity values are taken from Helgason and Pomeroy (2012). The value of h_s is chosen to be $5 \pm 5 \text{ cm}$ by visual inspection of the snow temperature measurements of Helgason and Pomeroy (2012).

The different heat fluxes are on the right-hand side of Eq. 1. They are all considered to be positive when the heat is transferred towards the surface, either from the atmosphere or the ground below. The first two terms, R_n and H , are the radiative and turbulent sensible heat fluxes. Their measurement during the course of the campaign is detailed in Sect. 2.2.

The third term, G , is the ground heat flux, i.e., the conductive heat flux from the ground through the snow layer (2). It was estimated using the following equation:

$$G = -\frac{\lambda_s}{d_s - h_s} (T_S - T_G), \quad (3)$$

with λ_s the snow conductivity and T_G the ground temperature. Here, T_G is considered to be constant $= -2 \pm 2 \text{ }^\circ\text{C}$ throughout our period of study. This is supported by the fact that soil temperature at the the Ameriflux US-Uaf site (Ueyama et al. 2018), only around 1.5 km away from the UAF Field, varied only from -2.5 to $-0.5 \text{ }^\circ\text{C}$ from 26 November to 14 December 2019. The snow conductivity is considered to be $\lambda_s = 0.2 \pm 0.05 \text{ W m}^{-1} \text{ K}^{-1}$, which was the value chosen by Helgason and Pomeroy (2012) in quite similar conditions. The error in G was calculated by propagating the errors on λ_s , d_s , h_s , and the temperatures.

The last term, L , is the turbulent latent heat flux, which was not measured but was assumed to be negligible, at least over the case study (4–8 December) period. This is supported by the low specific humidity and very cold weather, which lead to low saturation specific humidity. For example, on 6 December 0000 UTC, the radiosonde at the Fairbanks airport measured a specific humidity of $4.7 \times 10^{-4} \text{ kg kg}^{-1}$ while the surface saturation specific humidity was $3.9 \times 10^{-4} \text{ kg kg}^{-1}$.

The last term, δE , is the residual or SEB closure. It encompasses a number of terms which are usually considered to be negligible, such as advection (horizontal and vertical) and the horizontal divergence of the turbulent sensible heat flux. In Sect. 4.4, δE is calculated as the difference between the heat storage and the other fluxes. The error on δE is calculated by propagating the flux errors.

2.2 Instruments and Data Treatment

The instrument characteristics and the main aspects of the data treatment are outlined below. The main instruments for measuring the energy fluxes and relevant physical quantities included a sonic anemometer and a radiometer, which were installed in a flat and homogeneous field at the UAF Campus Farm. A microlidar was installed in downtown Fairbanks near the CTC (Community & Technical College) building (Fig. 1). They were all installed and running from 26 November to 12 December (Table 1). Most statistics hereafter will be derived from this complete measurement period. The period from 4 to 8 December is

Table 1 Summary of the different instruments installed during the pre-ALPACA 2019 winter campaign and of the associated measured variables

Instrument	Operation date	Location	Measured variables
Campbell Scientific 107 Temp. probe	04/12/2019–10/12/2019	UAF field	Temperature @ 2 m
RMYoung 81000 3D sonic anemometer	26/11/2019–15/12/2019 (**)	UAF field	Wind speed @ 2 m Wind direction @ 2 m Turbulent sensible heat flux
Kipp&Zonen CNR4 net radiometer	25/11/2019–12/12/2019	UAF field	↑ ↓ Longwave radiative flux ↑ ↓ Shortwave radiative flux
CIMEL CE376 micro-lidar (MILAN)	24/11/2019–13/12/2019	CTC building	Cloud base Cloud optical depth ($\lambda = 532$ nm)
Radiosonde (*)	Daily at 0000 & 1200 UTC	Fairbanks airport	Temperature profile Wind speed and dir. profile

(*) The radiosonde data was taken from the University of Wyoming website: <http://weather.uwyo.edu/upperair/sounding.html>. (**) The sonic anemometer was installed on 26/11 but data from 26/11 to 30/11 was excluded due to acquisition issues

of particular interest because synoptic conditions were favourable to the development of a surface-based temperature inversion (Sect. 3).

2.2.1 Sonic Anemometer

The sonic anemometer measured the temperature and the three components of the wind field at 10 Hz frequency. A separate thermometer deployed on the mast at approximately 2 m height during the 4–10 December period was used to calibrate the sonic temperature.

The 10 Hz measurements are despiked (Vickers and Mahrt 1997), and then averaged over fixed 30 min intervals to obtain mean wind speed U , wind direction θ and temperature T_{2m} . The turbulent sensible heat flux is also calculated over these intervals, following a procedure detailed in Fochesatto et al. (2013).

Quality control of the sonic anemometer measurements of H is ensured by applying the stationarity test of Foken and Wichura (1996). We then exclude from further analysis 30 min periods, which are shown to be non-stationary. This represents 48% of the measurement periods. The relative error on H is estimated at 30% following Weill et al. (2012).

2.2.2 Lidar

MILAN is a micro-lidar produced by Cimel Electronique (CE376), which is specialized for the study of tropospheric clouds and aerosols. It operates at two wavelengths, one in the visible spectrum (green: 532 nm) and one in the near infrared (808 nm), and measures polarization. Here, only the profiles at the 532-nm wavelength were analyzed. Indeed, the

objective was the detection of clouds, for which one wavelength is sufficient. Furthermore, the green source was more powerful and offered a greater vertical range: greater than 10 km in night-time conditions, i.e., a majority of the time in Fairbanks in December. Acquired profiles are averaged over 10 min to reduce noise while keeping information on cloud cover variability. The exploitable measurements were limited to altitudes above 210 m. Cloud-layer base and optical depth are obtained using the procedure detailed in Maillard et al. (2021).

For each profile, the optical depths of all detected cloud layers are summed to yield a total optical depth value τ . The lowest layer base altitude B is also calculated. If no layer is present, then B is indicated as missing data. Both B and τ are then averaged over the three profiles that occur during each sonic anemometer 30-min measurement period. A 30-min measurement period is determined to be ‘clear’ if $\overline{B} > 8$ km or $\overline{\tau} < 0.2$. This accounts for 29% of measurement periods. On the other hand, it is deemed to be ‘cloudy’ if $\overline{B} < 500$ m or $\overline{\tau} > 0.8$. This occurs a further 42% of the time. Indeterminate cases make up the remaining 29% of measurement periods.

2.2.3 Radiometer

The CNR4 Net Radiometer produced by Kipp & Zonen is composed of two pyranometers–pyrgeometer pairs, one nadir looking to measure the upwelling fluxes and one zenith looking to measure the downwelling fluxes. The pyranometers measure the radiation in the 300–2800 nm spectral range, while the spectral range of the pyrgeometers is 4.5–42 μ m. The total net radiative flux R_n is equal to $LW_n + SW_n$, with LW_n the net longwave flux and SW_n the net shortwave flux, and is positive when heat is transferred to the ground.

The surface temperature T_s can also be calculated from the radiometer measurements:

$$T_s = \left(\frac{LW_u - (1 - \epsilon)LW_d}{\epsilon\sigma_{SB}} \right)^{1/4}, \quad (4)$$

with LW_u and LW_d the upwards and downwards longwave radiative fluxes measured by the radiometer, ϵ the snow emissivity and $\sigma_{SB} = 5.67 \times 10^{-8} \text{ W m}^{-2} \text{ K}^{-4}$ the Stefan–Boltzmann constant. The snow emissivity is chosen equal to 0.99 in accordance with Weill et al. (2012).

Measurements were made every minute and averaged over 30-min periods in order to match the turbulent flux measurements (Sect. 2.2.1). The error on R_n is estimated from the 30-min period standard deviations of the individual radiative flux components, with a minimum of 5 W m^{-2} .

2.3 Other Available Datasets

Radiosondes are launched twice a day, at 0000 and 1200 UTC at the Fairbanks International Airport (Fig. 1). The wind and temperature profiles from these radiosonde launches were retrieved from the University of Wyoming website (Table 1). The near-surface temperature gradient is calculated from the first two levels of radiosonde data. The first level is at the surface, while the second level varied in altitude from 12 to 171 m (median: 22 m, mean: 43 m) over the course of the campaign.

ERA5 is the latest reanalysis from the European Centre for Medium-Range Weather Forecast (Hersbach et al. 2020). It provides hourly or four-times-daily estimates of many weather variables on a $0.25^\circ \times 0.25^\circ$ grid and with 137 vertical pressure levels. Values of geopotential, temperature and winds at the 700 hPa level over Alaska are used to discuss the synoptic situation. Hourly estimates of surface level variables such as temperature and wind

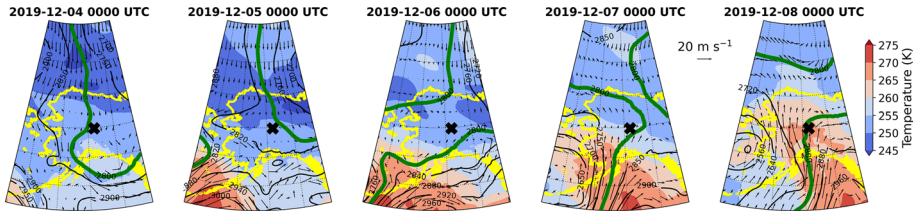


Fig. 3 Maps of the ERA5 geopotential height (contours), winds (arrows) and temperature (colours) at 700 hPa from 4 December 2019 to 8 December 2019 at 0000 UTC. The wind and temperature scales are the same for each plot and are indicated on the right. The bold green line marks the 2800 m contour of geopotential height. The yellow line marks the Alaskan coastlines and the black cross indicates the location of Fairbanks

speeds are also provided. Time series of these variables at the nearest grid point to Fairbanks (64.75°N , -147.75°W) were extracted for comparison to the UAF Field site measurements (Sect. 4.1).

3 Local Variability in Surface-Based Inversion Development: A Case Study

3.1 Evolution of a Surface-Based Inversion at Fairbanks Airport

From 4 to 8 December 2019, the buildup, then breakup, of a surface-based temperature inversion at Fairbanks airport was observed. The evolution of the inversion is visible in the profiles obtained at the airport from radiosonde launches and can be divided into three phases:

- From 4 to 5 December 0000 UTC, an anticyclone was positioned over central Alaska (Fig. 3). High pressures and subsidence led the cloud layer to decrease in altitude from 3 km to less than 2 km (Fig. 4a) while the air column cooled as a whole (Fig. 5a). As is frequent in anticyclonic conditions, synoptic winds were weak and wind speeds close to the ground remained under 2 m s^{-1} (Fig. 5b).
- From 5 to 6 December 0000 UTC, clouds were absent and the surface net radiative flux was strongly negative (Fig. 4e). This led to the surface continuing to cool while the air above 80 m stayed at a near-constant temperature (around -20°C), therefore creating a strong temperature gradient near the surface (Fig. 5c). This gradient was strongest around 1200 UTC on 6 December, when the surface temperature at the airport reached a minimum of -30°C .
- From 7 December, a pressure dipole is installed over south Alaska and funnels warm air from the Gulf of Alaska to Interior Alaska (Fig. 3). Consequently, heat advection was positive over Fairbanks (from ERA5 reanalyses, not shown), wind speeds increased above 500 m altitude, and the whole column started to warm again. At the end of 7 December, clouds returned and the net radiative flux at the surface became positive again (Fig. 4a, e). The surface then began to warm rapidly (Fig. 5c). The surface inversion at Fairbanks airport was completely erased on 8 December 1200 UTC.

The observed evolution of the surface-based temperature inversion at the airport was therefore largely controlled by the synoptic conditions. Its development was triggered by anticyclonic, subsident conditions that favour strong radiative cooling at the surface, and it was destroyed by an east–west pressure dipole advecting warm air and clouds from the south.

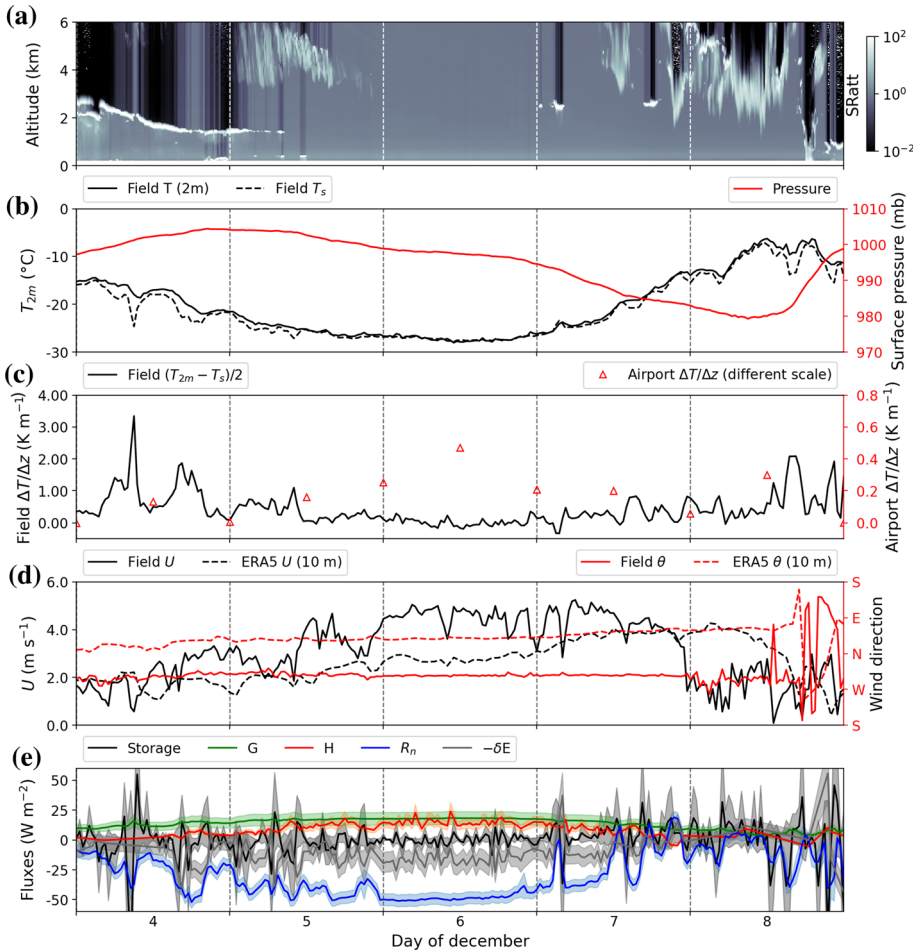


Fig. 4 Time series of the measurements from 4 to 8 December 2019 at Fairbanks. **a** Attenuated scattering ratio (SR_{att}) from the MILAN lidar. **b** 2 m temperature (continuous black) surface temperature (dashed black) and surface pressure (red) measured at the UAF Field. **c** Near surface temperature gradient from the radiosonde measurements (right axis) and the field measurements (left axis). Note the different scales for both measurements. **d** Continuous lines represent the wind speed U (black) and wind direction θ (red) measured by the sonic anemometer at the field. Dashed lines represent the same variables at 10 m from the ERA5 reanalysis. **e** Measured and estimated terms of the surface energy budget (Eq. 1) at the UAF Field site. Shown error bars correspond to the uncertainties which are estimated as in Sect. 2.2. For greater readability, the opposite of the residual ($-\delta E$) has been represented

3.2 Surface Energy Fluxes and Temperature Gradient at the Field Site

The temperature gradient measured at the UAF Field site did not follow the same evolution as the airport. Instead, $\Delta T = T_{2m} - T_s$ decreased from 4 December and remained low from 5 to 7 December (Fig. 4c). A direct comparison between the two measurements is complicated because while the UAF Field ΔT is the difference between the air temperature at 2 m and the snow surface temperature, the radiosondes measure only the air temperature at the surface and at a second launch-dependent altitude. From 5–7 December this second altitude varied from

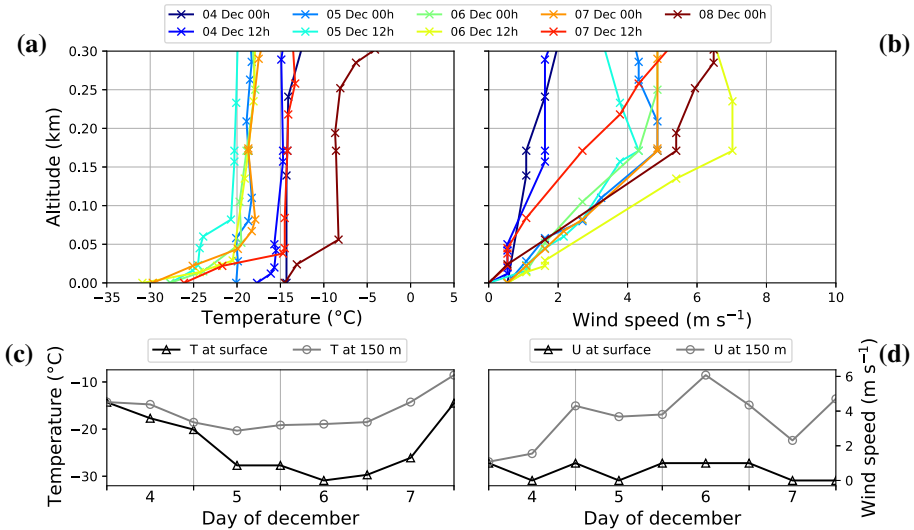


Fig. 5 Radiosonde profiles of dry-bulb temperature (a) and wind speed (b) from the Fairbanks airport for the period from 4 December 0000 UTC to 8 December 0000 UTC. (c, d) show the time evolution of the temperature and wind speed respectively, at the surface and at 150 m, as interpolated from the radiosonde data

14 to 28 m (mean: 20 m). The airport $\Delta T/\Delta z$ therefore represents a more vertically averaged gradient, which explains that it is smaller in magnitude than the field $\Delta T/\Delta z$ (Fig. 4c). It is possible that the rather coarse radiosonde vertical resolution “hides” a neutral gradient layer in the first 2 m, similar to what is observed at the field. However, this does not seem likely for two reasons. First, in the case of a radiatively driven SBI, such as the one occurring at the airport, the temperature gradient is typically strongest close to the ground. Second, the surface air temperature is around 3 °C colder at Fairbanks airport than at the UAF Field site. In any case, there is a markedly different trend between the small-scale UAF Field and the more vertically averaged Fairbanks airport temperature gradients, the former decreasing while the latter increases.

This ΔT trend at the UAF Field site appears to be linked to the wind speed. In contrast to the airport, where the surface wind speed remained low close to the surface from 4 to 8 December, the field wind speed increased from 3 December and was maximum from 5 to 7 December at the UAF Field site, before collapsing on 8 December (Fig. 4d). Physically, this is expected to have an impact on both H and ΔT , because increased wind shear leads to an increase in turbulent mixing. This in turn heightens H and tends to mechanically return the temperature profile to a neutral gradient.

Indeed, H increased and ΔT decreased in parallel to the increase in wind speed from 3 to 6 December (Fig. 6). The opposite evolution then took place from 7 to 8 December. Note that the fact that the turbulent sensible heat flux remained quite large on 7 December (Fig. 6) even though the surface ΔT was near zero implies that a temperature gradient persisting somewhere else in the air column was acting as a heat reservoir, perhaps affecting the surface through larger eddies (Mayfield and Fochesatto 2019). If the whole column were near neutral (i.e., well mixed), the turbulent sensible heat flux would be expected to collapse.

The 4–8 December episode indicates that there are important local variations in the development of SBIs. While the airport exhibited a strong temperature gradient and low wind

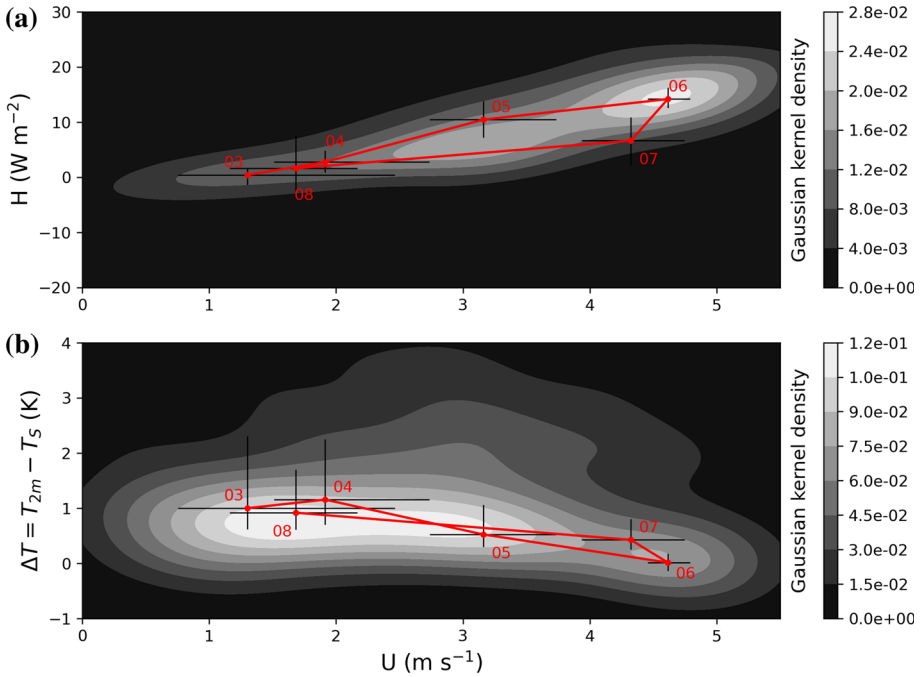


Fig. 6 **a** Turbulent sensible heat flux vs wind speed. The grey contours represent the Gaussian kernel density over the whole measurement period, i.e., lighter values denote greater point density. The red dots represent the median measurements for each day from 3 to 8 December (the date is labelled in red: the black horizontal and vertical bars represent 25th and 75th percentile). **b** The same, for ΔT as a function of wind speed

speeds directly linked to anticyclonic synoptic conditions, the UAF Field site had higher wind speeds and very small ΔT . In the next section, it will be shown that these higher wind speeds were caused by a local flow which influences the SEB and consequently affects the development of surface-based temperature inversions at the UAF Field site.

4 Impact of the Local Flow on the Surface Energy Budget and Temperature Gradient

4.1 Characterisation of the Local Flow

The presence of a local flow with particular characteristics has already been attested at this site by Fochesatto et al. (2013). They considered that this was a flow from the Goldstream Valley to the North (Fig. 1a), and suggested that it could be either a drainage flow triggered by strong radiative cooling of the Goldstream valley slopes or a channelling of the larger-scale, northerly synoptic flow through the mountain valleys. They defined ‘shallow cold flow’ (SCF) events as periods when the wind speed is greater than 1 m s^{-1} , the wind direction is north-westerly, and the winds are decoupled from the main meso-scale motion. During the pre-ALPACA campaign, a particular wind regime similar to the SCF was observed at the UAF Field site at a height of 2 m. Its characteristics are outlined below.

Firstly, the wind direction at the UAF Field site was largely north-westerly over the course of the campaign, with 50% of values between 293° and 305° . This orientation indicates a flow coming from the Goldstream Valley (Fig. 1). This is in contrast to the ERA5 values at the nearest grid point, which are north-easterly (e.g., Fig. 4d). These are assumed to be representative of larger-scale flows, as ERA5 has a 0.25° resolution and is not able to capture a local circulation from the Goldstream valley. Furthermore, while the 64.75°N , -147.75°W model grid node is the closest to the UAF Field site, it is further south in the Tanana valley and would likely not be impacted by a flow from the Goldstream Valley.

Secondly, this wind was enhanced under clear sky conditions. For periods identified as clear by the lidar (Sect. 2.2.2), the median wind speed is 3.9 m s^{-1} and 90% of wind directions are between 292° and 310° . On the other hand, for periods identified as cloudy, the median wind speed is 2.2 m s^{-1} , with a larger scatter in wind direction. The difference between wind speed distribution under clear and cloudy conditions is different at a statistically significant level: Mann–Whitney $U = 32189$, p value $< 10^{-3}$ for sample sizes of 256 and 385 respectively (Mann and Whitney 1947).

This wind regime is highlighted in the case study described in Sect. 4. Wind speeds at the UAF Field site increased to more than 5 m s^{-1} under subsident, clear-sky conditions and the wind exhibited a consistent north-westerly direction. The orientation relative to the topography and the association with clear-sky periods suggests that this flow is a sort of drainage or topography-driven flow. However, we lacked the measurements necessary to establish either its origin or its spatial extent robustly. For this reason, it will be termed ‘local flow’ (LF) to avoid conflating it with the SCF of Fochesatto et al. (2013). In Sect. 4.2, the impact of this LF on the surface energy balance at the UAF Field site is explored.

4.2 Identification of Two Distinct Modes in the Surface Energy Budget

Previous studies have shown that the net longwave radiative flux at the surface is bimodal during the Arctic winter (Stramler et al. 2011; Graham et al. 2017). The first mode is around -40 W m^{-2} and is associated with the absence of low-level, high-emissivity clouds, while the second mode is around 0 W m^{-2} and is associated with their presence. Here, individual 30-min measurement periods are defined as ‘clear’ or ‘cloudy’ based on the lidar observations (Sect. 2.2.2). Net longwave flux measurements are distributed around -45 W m^{-2} during clear periods, and around -5 W m^{-2} during cloudy periods, in good agreement with previous high-latitude observations. Because SW_n is negligible during this period, this is also true of the net radiative flux (Fig. 7a). The overlap between the two modes is quite small, and the total distribution of R_n is bimodal.

The turbulent sensible heat flux depends on the wind speed (Sect. 3.2). Values of H are distributed around 0 W m^{-2} when the wind speed is less than 2 m s^{-1} . On the other hand, when the wind speed is greater than 3 m s^{-1} , H is distributed around 12 W m^{-2} . The spread is larger in this second mode, so that the overlap between the two is slightly larger than for the radiative fluxes (Fig. 7b). However, the two distributions are still different at a statistically significant level. The Mann–Whitney U -test (Mann and Whitney 1947) yields a p value $< 10^{-10}$ (the sample sizes of the two distributions are 255 and 58 and the test statistic, U , is = 1039). These values are comparable in magnitude to those measured by Fochesatto et al. (2013) at the same site in the absence and presence of the SCF.

These net radiative and turbulent sensible heat flux modes are linked (Fig. 7c). The Gaussian kernel density (grey field contours) of measurements during the pre-ALPACA campaign show that there are two modes in the (H, R_n) space. The first corresponds to $R_n \approx -5\text{ W m}^{-2}$

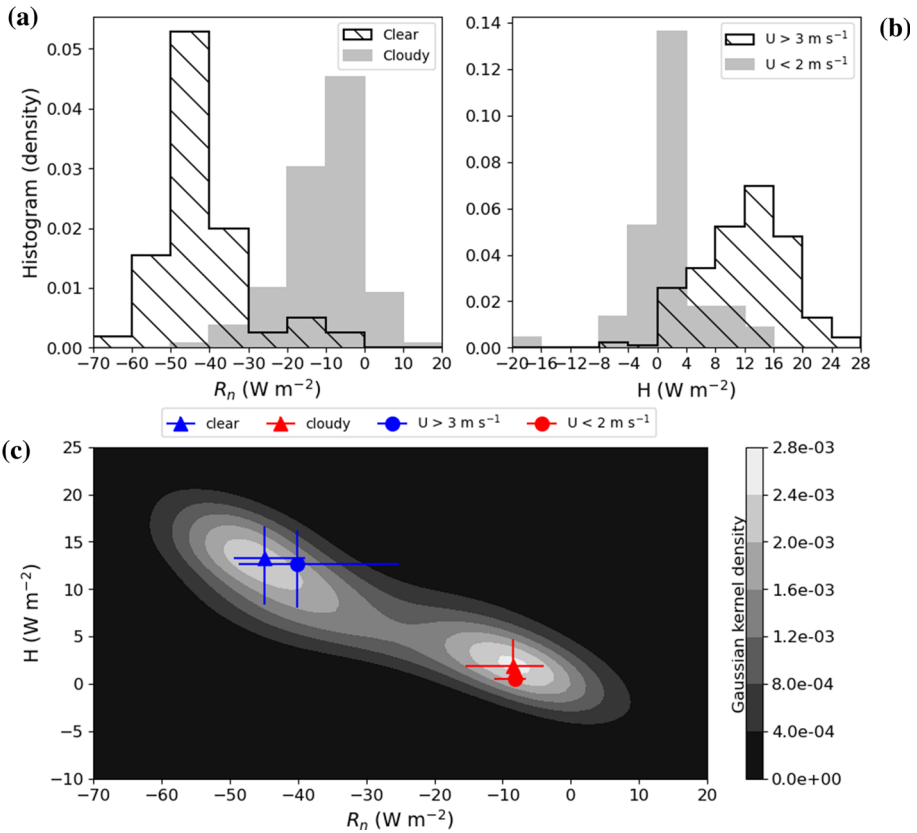


Fig. 7 Top panels: histograms of **a** the net radiative flux (R_n) in the presence (grey) and absence of clouds (hatched black) and **b** the turbulent sensible heat flux in high (hatched black) and low (grey) wind speed conditions respectively. **c** The grey scale represents the calculated gaussian kernel point density in the (R_n, H) space. The symbols represent the median (R_n, H) pair for either clear (blue triangle) or cloudy (red triangle) conditions, and for wind speeds less than 2 m s^{-1} (red circles) or more than 3 m s^{-1} (blue circle). The errorbar corresponds to the 25th and 75th percentiles. These statistics were drawn from the entire campaign period

and $H \approx 0 \text{ W m}^{-2}$ and the second corresponds to $R_n \approx -45 \text{ W m}^{-2}$ and $H \approx 14 \text{ W m}^{-2}$. This reflects the observed association between clear skies and the presence of an enhanced LF (Sect. 4.1). Indeed, measurements that correspond to cloudy periods or low wind speeds are clustered in the first mode while measurements corresponding to clear instants or high wind speeds are clustered in the second mode (Fig. 7c). It should be noted that some measurement periods with U greater than 3 m s^{-1} also have a net radiative flux well within the cloudy mode, leading to the larger error bars associated with the blue circle (Fig. 7c). This is because while high wind speeds are generally associated with clear skies at the UAF Field site, they sometimes persist throughout short periods of cloudiness—for example, on 7 December (Fig. 4c).

Schematically, the SEB at the UAF Field site exhibits two preferred modes. The first, with near zero radiative and turbulent heat fluxes, is linked to cloudy skies and weak winds. The second, with very strongly negative radiative fluxes and high turbulent heat fluxes, is linked to clear skies and higher local wind speeds due to the presence of the LF. The conjunction

of clear skies/low R_n and low wind speeds/low H occurs more rarely. The formation of a surface-based temperature inversion at the field is therefore a balancing act. On the one hand, clear skies and high pressures create a large negative R_n , which is necessary for the surface to begin cooling. On the other, the same situation has the potential to strengthen the LF, which tends to destroy the inversion by increasing mixing due to stronger wind shear. This mechanism is explored in more detail in Sect. 4.3.

4.3 The Local Flow Dampens the Effect of Strong Radiative Cooling

Recent studies have introduced the concept of a critical wind speed separating two distinct turbulence regimes, often termed ‘weakly’ and ‘strongly’ stable (Sun et al. 2012, 2016). Here, the impact of the wind speed on the surface inversion response to strong radiative cooling is examined. For $R_n > -15 \text{ W m}^{-2}$, ΔT was observed to increase slowly with decreasing net radiative flux at the UAF Field site (Fig. 8). The rate of increase is the same for all wind speeds, i.e., around $-0.06 \text{ K W}^{-1} \text{ m}^2$. However, for lower values of R_n , the effect of the net radiative heat flux on the surface-based temperature inversion strongly depends on the wind speed. For $U > 3 \text{ m s}^{-1}$, ΔT is independent of R_n (the slope is $0.02 \text{ K W}^{-1} \text{ m}^2$, but the decrease is non-significant in light of the error bars). This is coherent with the weakly stable regime. As the shear at these higher wind speeds generates enough turbulent sensible heat flux to make up for the radiative loss, ΔT is not sensitive to the value of R_n and remains close to zero. In other terms, the air from 0 to 2 m is well mixed. Note that the red outliers at $R_n > 10 \text{ W m}^{-2}$ correspond to 30-min measurement periods when short-lived clouds passed over the UAF Field site on 7 December, leading to a temporary elevation of R_n at continued low ΔT . For U lower than 2 m s^{-1} , on the other hand, ΔT increases sharply with decreasing net radiative flux, at a rate of $-0.11 \text{ K W}^{-1} \text{ m}^2$. This is the expected evolution in the strongly stable regime. Indeed, this regime is radiatively driven: the turbulent sensible heat flux cannot compensate for the strongly negative radiative flux, and so the equilibrium ΔT will depend on the magnitude of the radiative imbalance.

The presence of the LF at the UAF Field site therefore controls the response of the stability to strong radiative cooling conditions. Qualitatively, in clear sky conditions, the regime is strongly stable when U is under 2 m s^{-1} and weakly stable when U is over 3 m s^{-1} , with a critical wind speed in the $2\text{--}3 \text{ m s}^{-1}$ interval. This represents a new finding in the Arctic context. At Dome C in the Antarctic, Vignon et al. (2017) found a critical 10 m wind speed threshold between 5 and 7 m s^{-1} . Below, this value will be compared to theoretical predictions.

It has been shown that the critical wind speed depends on the surface radiative flux (van de Wiel et al. 2012). This is because the shear necessary to create the sensible heat flux compensating a very large radiative deficit will be higher than if it is close to 0 W m^{-2} . To be more precise, the turbulent sensible heat flux must not compensate R_n , but its difference with van Hooijdonk et al. (2015) derive the following expression for the critical wind speed:

$$U_{\min} = \left(\frac{27\alpha}{4} \right)^{1/3} \left\{ \frac{g}{\theta_0 \kappa^2} \frac{(|R_n| - |G|)}{\rho_a C_{p,a}} z [\ln(z/z_0)]^2 \right\}^{1/3}, \quad (5)$$

with α the stability parameter, $g = 9.81 \text{ m s}^{-2}$ the acceleration due to gravity, θ_0 the air potential temperature, $\kappa = 0.4$ the von Kármán constant, G the ground flux, and $z = 2 \text{ m}$ the altitude above the surface. The roughness length z_0 chosen here was 10^{-4} m , which is typical of relatively flat, snow-covered surfaces (Weill et al. 2012; Helgason and Pomeroy 2012). Here, we consider values of $\theta_0 = 250 \text{ K}$ and $\alpha = 4$, inline with van de Wiel et al. (2012).

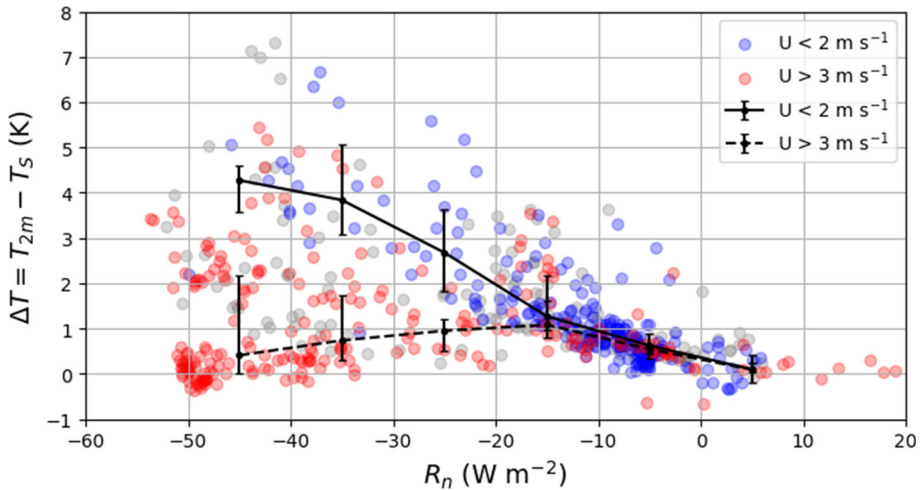


Fig. 8 Surface temperature gradient (ΔT) as a function of the net radiative flux at the UAF Field site. The two lines correspond to the medians for each 10 W m^{-2} bin, for wind speeds of less than 2 m s^{-1} (blue points) and more than 3 m s^{-1} (red points) respectively. Grey points correspond to U between 2 and 3 m s^{-1} . Error bars denote the 25th and 75th percentiles; these statistics were drawn from the entire campaign period

Equation 5 shows that U_{\min} increases monotonously with the heat demand at the surface, i.e., $|R_n| - |G|$. The value of U_{\min} is between 2 and 3 m s^{-1} for values of the heat demand at the surface between 8 and 25 W m^{-2} , which is the case for 46% of the measurements where $R_n > -15 \text{ W m}^{-2}$. If the heat demand is between 25 and 40 W m^{-2} , then U_{\min} is between 3 and 3.5 m s^{-1} . This corresponds to a further 43% of measurements where the net radiative flux is less than -15 W m^{-2} . In total, 89% of measurements with $R_n < -15 \text{ W m}^{-2}$ would have a theoretical critical wind speed greater than 2 m s^{-1} according to Eq. 5.

These theoretical values of the critical wind speed are coherent with the observed behaviour illustrated in Fig. 8. For net radiative fluxes at the surface lower than -15 W m^{-2} , the theoretical critical wind speed is overwhelmingly over 2 m s^{-1} . This explains that wind speeds lower than 2 m s^{-1} at the UAF Field site correspond to a strongly stable regime, where the near surface inversion increases sharply with decreasing net radiative flux at the surface. However, a significant fraction of the measurement periods have a theoretical critical wind speed greater than 3 m s^{-1} . Qualitatively, this fits with the large spread of values for $R_n < -30 \text{ W m}^{-2}$ and $U > 3 \text{ m s}^{-1}$ (red points) in Fig. 8. The criterion “ $U > 3 \text{ m s}^{-1}$ ” is not sufficient to guarantee that the wind speed is above the critical threshold, thus leading to the observed large number of outliers overlapping with blue points at $R_n < -30 \text{ W m}^{-2}$.

The use of Eq. 5 as a comparison to our data raises two issues. Firstly, it is obtained by supposing that Monin–Obukhov hypothesis holds true, and that the wind profile is logarithmic. These conditions might not hold when the LF is occurring at the UAF Field site, if it is a drainage flow with a wind maximum very close to the ground. Secondly, Eq. 5 implicitly supposes that there is no significant residual in the SEB. The magnitude of the residual and its potential link to advection is explored in Sect. 4.4.

4.4 Surface Energy Budget Closure

Over the course of the campaign, the residual was found to have a median value of 13 W m^{-2} , with 90% of values falling between -4 and 29 W m^{-2} (note that for reasons of readability, $-\delta E$ is represented on Fig. 4e). The residual is therefore largely positive, indicating a missing heat transfer from the atmosphere to the ground which is particularly large (median 19 W m^{-2}) during clear periods. In contrast, the median residual was only around 2 W m^{-2} for cloudy periods. This is because the ground and turbulent sensible heat fluxes cannot make up for the very strongly negative R_n of clear periods. In the following discussion the lack of closure in the case study period is examined in more detail. Figure 4e shows that the residual is almost as large as the ground and turbulent heat fluxes from 5 to 7 December (around 18 W m^{-2}), although the error bars are large.

This is not an unusual observation in an Arctic context. Similar values of the residual (18 W m^{-2}) were also obtained in comparable conditions (Arctic night) by Helgason and Pomeroy (2012). The dataset in their study was more complete as regards latent heat fluxes and ground heat fluxes and the residual was found to be outside of random measurement errors. Reviewing possible sources of systematic measurement errors, the authors concluded that non-turbulent exchanges of sensible heat between air and snow could be of importance given the strong correlation between the temperatures of near-surface air and snow. However, such an exchange of heat would not impact the energy balance of the system as defined in Sect. 2.1, since the top 5 cm of snow are already supposed to be in thermodynamic equilibrium with the air. Increasing h_s to 10 or even 20 cm has negligible impact on the residual during the case study, as the surface temperature changed little during this time. Another possibility evoked by Helgason and Pomeroy (2012) is that a strong temperature gradient in the lowest metres would cause a turbulent sensible heat flux divergence between the surface and the measurement height, so that the measured H would not be representative of its surface value. This seems unlikely here as ΔT is close to 0 K over this period when the residual is highest.

Other possible sources of systematic error on the SEB include the presence of eddies with timescales larger than the 30-min period used for calculation of the turbulent sensible heat flux (Malhi et al. 2005; Mauder et al. 2020). Indeed, the detrending method outlined in Sect. 2.1 acts as a high-pass filter with a cutoff at 30 min. Neglecting lower-frequency transport of sensible heat would lead to an underestimation of H , and therefore a lack of heat at the surface such as is observed here. However, visual inspection of the cospectra of vertical wind and temperature does not support this conclusion, with exchanges of heat appearing to be minimal at timescales greater than 30 min (not shown). The footprint of the eddy-covariance measurement is another possible issue. Fochesatto et al. (2013) compared measurements of H at the UAF Field site obtained by a sonic anemometer and a large-aperture scintillometer (LAS) and found that the sonic anemometer captured around 75% of the flux measured by the LAS. Since the LAS measurement is an integral over an approximately 500 m line, this suggests that the representativeness of the sonic anemometer footprint might be an issue. However, correcting the ALPACA 2019 measurements to account for this effect only reduces the residual by around 5 W m^{-2} .

Lastly, we consider the possibility that the residual is due to advection, either vertical or horizontal. Previous studies have shown that vertical advection may cause important heat fluxes even for vertical velocity components below the instrumental measurement capabilities (a few cm s^{-1}) when the vertical temperature gradient is large (Nakamura and Mahrt 2006; Leuning et al. 2012), which is not the case during the case study. Therefore it is unlikely that vertical advection could explain the 18 W m^{-2} residual during this period. On the other

hand, large residuals occurred in clear-sky conditions during the entire campaign, and clear sky conditions coincided with heightened horizontal wind speeds ($U > 3 \text{ m s}^{-1}$).

The horizontal temperature gradient needed to explain the entire residual is calculated, following Leuning et al. (2012) as:

$$\frac{\partial T}{\partial x} = \frac{\delta E}{h_a \rho_a C_{p,a} U/2}, \quad (6)$$

with $h_a = 2 \text{ m}$ the altitude of the instruments, and U the wind speed. Leuning et al. (2012) use $U/2$ to approximate the mean wind speed in the layer between the surface and h_a . Using $U = 5 \text{ m s}^{-1}$ and $\delta E = 18 \text{ W m}^{-2}$, Eq. 6 yields a horizontal temperature gradient of 3 K km^{-1} . This is unrealistically large. However, for the LF where the wind speed maximum might be close to the ground and the roughness length is small, the mean wind speed between 0 and h_a may be closer to U than $U/2$. In that case, the necessary horizontal temperature gradient to close the SEB would be only 1.5 K km^{-1} .

As there unfortunately were no along-flow wind and temperature measurements during the campaign, the true value of advection cannot be estimated.

5 Conclusions and Perspectives

This paper analyzed observations from the pre-ALPACA 2019 winter campaign, which took place from 23 November to 12 December 2019 in Fairbanks, Alaska, and investigated the impact of a local flow on the surface energy balance and surface-based temperature inversion development.

First, a case study highlighting the studied phenomenon was introduced. In the days leading up to 5 December 2019, high synoptic caused subsidence in the upper levels of the troposphere, leading to the disappearance of clouds through adiabatic compression and largely negative (less than -50 W m^{-2}) net radiative fluxes in Fairbanks. A strong surface-based temperature inversion was observed to develop at the airport over this period, while surface level wind speeds remained low (under 2 m s^{-1}). At the UAF Field measurement site, in contrast, the wind speed was seen to increase on 5 December to values greater than 5 m s^{-1} . The turbulent sensible heat flux increased in parallel, while the near surface temperature gradient ($\Delta T = T_{2\text{m}} - T_S$) decreased. On 6 December, the temperature gradient reached its maximum at the airport and its minimum at the UAF Field site, suggesting that different processes are operating at the two measurement sites.

The whole campaign dataset was then analyzed. It was shown that a particular wind regime, termed Local Flow (LF), occurred at the UAF Field measurement site. The LF was characterized by a consistent north-westerly wind direction, corresponding to the output of the Goldstream Valley. It was greatly enhanced under clear sky conditions: wind speeds were significantly higher at the UAF Field site in the absence of clouds than in their presence.

The association of clear skies and increased wind speeds was significant because wind speed is an important factor in determining the stability regime. When the wind speed was less than 2 m s^{-1} , the surface ΔT increased strongly with decreasing net radiative flux, leading to a radiatively controlled strongly stable regime for R_n less than -30 W m^{-2} . On the other hand, when wind speeds were greater than 3 m s^{-1} , turbulence could be sustained even for very strongly negative net radiative fluxes (weakly stable regime). The resulting mechanical mixing meant that the near surface temperature gradient remained close to zero. Due to the LF, this was the most frequent scenario under clear skies at the UAF Field site.

The surface energy budget at the UAF Field site thus exhibited two preferred modes over the course of the campaign. The first mode was associated with low winds and the presence of clouds. The net radiative flux was around -5 W m^{-2} while the turbulent sensible heat flux was around 0 W m^{-2} , and the SEB residual was small. The second mode was characterized by elevated wind speeds and clear skies. The net radiative flux was approximately -45 W m^{-2} and the turbulent sensible heat flux around 13 W m^{-2} . In this second mode, the residual of the SEB was positive beyond the scope of random measurement errors, indicating a missing positive heat flux at the surface. For the 5–7 December episode, we estimate that a horizontal temperature gradient of $1.5\text{--}3 \text{ K km}^{-1}$ would account for the residual through horizontal heat advection by the LF.

In summary, the results presented here have shown that small-scale flows can penetrate stable cold air pools in the Arctic, such as the Tanana Valley, and locally modify the SEB and stability regime. This is potentially important for studies of local air pollution at high-latitudes since pollution episodes occur during cold, stable conditions. However, open questions remain concerning the dynamic characteristics of this flow and the representativeness of the UAF Field measurement site. Temperature profiles up to 50 m would help to characterize the surface inversion development and the turbulent mixing scales. A tighter network of instruments, both at the UAF Field and in the wider Fairbanks area, would make it possible to assess the origin and horizontal dimensions of the LF once it penetrates the Tanana Valley as well as to estimate heat advection.

Acknowledgements The authors would like to thank the other participants of the pre-ALPACA 2019 campaign for their help in setting up the instruments. In particular, thanks to B. Simpson and J. Mao for the logistical support at the UAF. Thanks also to T. Roberts for stimulating discussions about the findings. The authors acknowledge funding from the French Centre National de la Recherche Scientifique (CNRS) program LEFE (Les Enveloppes Fluides et l'Environnement), the French Polar Institute Paul-Emile Victor (IPEV), and the ANR CASPA (Climate relevant Aerosol Sources and Processes in the Arctic, ANR-2021-CE01-0017). Computer analyses benefited from access to IDRIS HPC resources (GENCI allocation A009017141) and the IPSL mesoscale computing centre (CICLAD: Calcul Intensif pour le Climat, l'Atmosphère et la Dynamique). G. J. Fochesatto was supported by NSF-PDM award 2146929. The datasets generated and analyzed during the current study are available from the corresponding author on reasonable request.

Open Access This article is licensed under a Creative Commons Attribution 4.0 International License, which permits use, sharing, adaptation, distribution and reproduction in any medium or format, as long as you give appropriate credit to the original author(s) and the source, provide a link to the Creative Commons licence, and indicate if changes were made. The images or other third party material in this article are included in the article's Creative Commons licence, unless indicated otherwise in a credit line to the material. If material is not included in the article's Creative Commons licence and your intended use is not permitted by statutory regulation or exceeds the permitted use, you will need to obtain permission directly from the copyright holder. To view a copy of this licence, visit <http://creativecommons.org/licenses/by/4.0/>.

References

- Bintanja R, van der Linden EC, Hazeleger W (2011) Boundary layer stability and arctic climate change: a feedback study using EC-earth. *Clim Dyn* 39(11):2659–2673. <https://doi.org/10.1007/s00382-011-1272-1>
- Bourne S, Bhatt U, Zhang J, Thoman R (2010) Surface-based temperature inversions in Alaska from a climate perspective. *Atmos Res* 95(2):353–366. <https://doi.org/10.1016/j.atmosres.2009.09.013>
- Bradley RS, Keimig FT, Diaz HF (1992) Climatology of surface based inversions in the North American Arctic. *J Geophys Res*. <https://doi.org/10.1029/92jd01451>
- Fochesatto GJ, Mayfield JA, Starkenburg DP, Gruber MA, Conner J (2013) Occurrence of shallow cold flows in the winter atmospheric boundary layer of interior of Alaska. *Meteorol Atmos Phys* 127(4):369–382. <https://doi.org/10.1007/s00703-013-0274-4>

- Foken T, Wichura B (1996) Tools for quality assessment of surface-based flux measurements. *Agric For Meteorol* 78(1–2):83–105. [https://doi.org/10.1016/0168-1923\(95\)02248-1](https://doi.org/10.1016/0168-1923(95)02248-1)
- Graham RM, Rinke A, Cohen L, Hudson SR, Walden VP, Granskog MA, Dorn W, Kayser M, Maturilli M (2017) A comparison of the two Arctic atmospheric winter states observed during N-ICE2015 and SHEBA. *J Geophys Res Atmos* 122(11):5716–5737. <https://doi.org/10.1002/2016jd025475>
- Haid M, Gohm A, Umek L, Ward HC, Rotach MW (2021) Cold-air pool processes in the Inn Valley during Föhn: a comparison of four cases during the PIANO campaign. *Boundary-Layer Meteorol*. <https://doi.org/10.1007/s10546-021-00663-9>
- Helgason W, Pomeroy J (2012) Problems closing the energy balance over a homogeneous snow cover during midwinter. *J Hydrometeorol* 13(2):557–572. <https://doi.org/10.1175/jhm-d-11-0135.1>
- Hersbach H, Bell B, Berrisford P, Hirahara S, Horányi A, Muñoz-Sabater J, Nicolas J, Peubey C, Radu R, Schepers D, Simmons A, Soci C, Abdalla S, Abellan X, Balsamo G, Bechtold P, Biavati G, Bidlot J, Bonavita M, Chiara G, Dahlgren P, Dee D, Diamantakis M, Dragani R, Flemming J, Forbes R, Fuentes M, Geer A, Haimberger L, Healy S, Hogan RJ, Hólm E, Janisková M, Keeley S, Laloyaux P, Lopez P, Lupu C, Radnoti G, Rosnay P, Rozum I, Vamborg F, Villaume S, Thépaut JN (2020) The ERA5 global reanalysis. *Q J R Meteorol Soc* 146(730):1999–2049. <https://doi.org/10.1002/qj.3803>
- Leuning R, van Gorsel E, Massman WJ, Isaac PR (2012) Reflections on the surface energy imbalance problem. *Agric For Meteorol* 156:65–74. <https://doi.org/10.1016/j.agrformet.2011.12.002>
- Mahrt L, Vickers D, Nakamura R, Soler MR, Sun J, Burns S, Lenschow D (2001) Shallow drainage flows. *Boundary-Layer Meteorol* 101(2):243–260. <https://doi.org/10.1023/a:1019273314378>
- Maillard J, Ravetta F, Raut JC, Mariage V, Pelon J (2021) Characterisation and surface radiative impact of arctic low clouds from the Jaos field experiment. *Atmos Chem Phys* 21(5):4079–4101. <https://doi.org/10.5194/acp-21-4079-2021>
- Malhi Y, McNaughton K, Von Randow C (2005) Low frequency atmospheric transport and surface flux measurements. In: Lee X, Massman W, Law B (eds) *Handbook of micrometeorology: a guide for surface flux measurement and analysis*. Springer, Dordrecht, pp 101–118. https://doi.org/10.1007/1-4020-2265-4_5
- Malingowski J, Atkinson D, Fochesatto J, Cherry J, Stevens E (2014) An observational study of radiation temperature inversions in Fairbanks, Alaska. *Polar Sci* 8:24–39. <https://doi.org/10.1016/j.polar.2014.01.002>
- Mann HB, Whitney DR (1947) On a test of whether one of two random variables is stochastically larger than the other. *Ann Math Stat* 18(1):50–60
- Martínez D, Jiménez MA, Cuxart J, Mahrt L (2010) Heterogeneous nocturnal cooling in a large basin under very stable conditions. *Boundary-Layer Meteorol* 137(1):97–113. <https://doi.org/10.1007/s10546-010-9522-z>
- Mauder M, Foken T, Cuxart J (2020) Surface-energy-balance closure over land: a review. *Boundary-Layer Meteorol* 177(2–3):395–426. <https://doi.org/10.1007/s10546-020-00529-6>
- Mayfield JA, Fochesatto GJ (2013) The layered structure of the winter atmospheric boundary layer in the Interior of Alaska. *J Appl Meteorol Climatol* 52(4):953–973. <https://doi.org/10.1175/jamc-d-12-01.1>
- Mayfield JA, Fochesatto GJ (2019) The turbulence regime of the atmospheric surface layer in the presence of shallow cold drainage flows: Application of laser scintillometry. In: Barillé R (ed) *Turbulence and related phenomena*. Chap 5. IntechOpen, Rijeka. <https://doi.org/10.5772/intechopen.80290>
- Nakamura R, Mahrt L (2006) Vertically integrated sensible-heat budgets for stable nocturnal boundary layers. *Q J R Meteorol Soc* 132(615):383–403. <https://doi.org/10.1256/qj.05.50>
- Pithan F, Mauritsen T (2014) Arctic amplification dominated by temperature feedbacks in contemporary climate models. *Nat Geosci* 7:181–184. <https://doi.org/10.1038/ngeo2071>
- Rotach MW, Calanca P, Graziani G, Gurtz J, Steyn DG, Vogt R, Andretta M, Christen A, Cieslik S, Connolly R, Wekker SFJD, Galmarini S, Kadyrov EN, Kadyrov V, Miller E, Neiningen B, Rucker M, Gorsel EV, Weber H, Weiss A, Zappa M (2004) Turbulence structure and exchange processes in an Alpine Valley: the Riviera project. *Bull Am Meteorol Soc* 85(9):1367–1386. <https://doi.org/10.1175/BAMS-85-9-1367>
- Serreze MC, Kahl JD, Schnell RC (1992) Low-level temperature inversions of the Eurasian Arctic and comparisons with Soviet drifting station data. *J Climate*. [https://doi.org/10.1175/1520-0442\(1992\)005<0615:litiot>2.0.co;2](https://doi.org/10.1175/1520-0442(1992)005<0615:litiot>2.0.co;2)
- Simpson W, Law K, Schmale J, Pratt K, Arnold S, Mao J (2019) Alaskan layered pollution and chemical analysis (ALPACA) White Paper. University of Alaska Fairbanks. Technical report
- Stramler K, Genio ADD, Rossow WB (2011) Synoptically driven arctic winter states. *J Clim* 24:1747–1762. <https://doi.org/10.1175/2010jcli3817.1>
- Sun J, Mahrt L, Banta RM, Pichugina YL (2012) Turbulence regimes and turbulence intermittency in the stable boundary layer during CASES-99. *J Atmos Sci* 69(1):338–351. <https://doi.org/10.1175/jas-d-11-082.1>

- Sun J, Lenschow DH, LeMone MA, Mahrt L (2016) The role of large-coherent-eddy transport in the atmospheric surface layer based on CASES-99 observations. *Boundary-Layer Meteorol* 160(1):83–111. <https://doi.org/10.1007/s10546-016-0134-0>
- Ueyama M, Iwata H, Harazono Y (2018) AmeriFlux AmeriFlux US-Uaf University of Alaska, Fairbanks, Ver. 9-5. Ameriflux AMP (Dataset). <https://doi.org/10.17190/AMF/1480322>
- van de Wiel BJH, Moene AF, Jonker HJJ, Baas P, Basu S, Donda JMM, Sun J, Holtslag AAM (2012) The minimum wind speed for sustainable turbulence in the nocturnal boundary layer. *J Atmos Sci* 69(11):3116–3127. <https://doi.org/10.1175/jas-d-12-0107.1>
- van de Wiel BJH, Vignon E, Baas P, van Hooijdonk IGS, van der Linden SJA, van Hooft JA, Bosveld FC, de Rooze SR, Moene AF, Genthon C (2017) Regime transitions in near-surface temperature inversions: a conceptual model. *J Atmos Sci* 74(4):1057–1073. <https://doi.org/10.1175/jas-d-16-0180.1>
- van Hooijdonk IGS, Donda JMM, Clercx HJJ, Bosveld FC, van de Wiel BJH (2015) Shear capacity as prognostic for nocturnal boundary layer regimes. *J Atmos Sci* 72(4):1518–1532. <https://doi.org/10.1175/JAS-D-14-0140.1>
- Vickers D, Mahrt L (1997) Quality control and flux sampling problems for tower and aircraft data. *J Atmos Oceanic Technol* 14(3):512–526. [https://doi.org/10.1175/1520-0426\(1997\)014<0512:QCAFSP>2.0.CO;2](https://doi.org/10.1175/1520-0426(1997)014<0512:QCAFSP>2.0.CO;2)
- Vignon E, van de Wiel BJH, van Hooijdonk IGS, Genthon C, van der Linden SJA, van Hooft JA, Baas P, Maurel W, Traullé O, Casasanta G (2017) Stable boundary-layer regimes at Dome C, Antarctica: observation and analysis. *Q J R Meteorol Soc* 143(704):1241–1253. <https://doi.org/10.1002/qj.2998>
- Weill A, Eymard L, Vivier F, Matulka A, Loisil R, Amarouche N, Panel JM, Lourenço A, Viola A, Vitale V, Argentini S, Kupfer H (2012) First observations of energy budget and bulk fluxes at Ny Ålesund (Svalbard) during a 2010 transition period as analyzed with the BEAR station. *ISRN Meteorol* 2012:675,820. <https://doi.org/10.5402/2012/675820>

Publisher's Note Springer Nature remains neutral with regard to jurisdictional claims in published maps and institutional affiliations.